JOURNAL OF GEOPHYSICAL RESEARCH, VOL. ???, XXXX, DOI:10.1029/,

Spectral modeling of wave dissipation on opposing current

André J. van der Westhuysen

Hydraulic Engineering Unit, Deltares | Delft Hydraulics, Rotterdamseweg 185, 2629 HD Delft, The Netherlands.

André J. van der Westhuysen, Hydraulic Engineering Unit, Deltares | Delft Hydraulics, Rotterdamseweg 185, 2629 HD Delft, The Netherlands. Andre.vanderWesthuysen@deltares.nl

Abstract.

Hindcast studies for the Dutch Wadden Sea using the spectral wind wave model SWAN have shown the significant influence of currents on wave predictions in the tidal inlets. In following current, observations are typically well reproduced, but under strong opposing (but not blocking) current, wave heights are significantly overestimated. *Ris and Holthuijsen* [1996] propose that such overestimations are due to insufficient steepness dissipation of waves on opposing current. The present paper presents a new formulation for the enhanced breaking dissipation of waves on opposing current. Unlike the expression by *Ris and Holthuijsen* [1996], the proposed expression isolates the steepening effect of the opposing current on the waves, so that inherently steep young wind sea is not overly dissipated. This expression contains one additional unknown parameter, which was calibrated using laboratory observations. Validation of this enhanced dissipation term for field cases of the Amelander Zeegat tidal inlet (Dutch Wadden Sea) shows an improvement for opposing current situations in the tidal channel. For situations with following current, no significant deterioration in results is found. In particular, the results for the young wind sea on the tidal flats are not significantly affected, unlike with the expression of *Ris and Holthuijsen* [1996]. However, since the remaining dissipation terms in SWAN have been calibrated without this enhanced dissipation term, the addition of the proposed formulation results in some deterioration of the overall statistics.

1. Introduction

The spectral wind wave model SWAN [*Booij et al.* 1999] is widely used for the computation of wave fields over shelf seas, complex coastal areas and in shallow lakes. The accurate estimation of the nearshore wave processes in this model is important to various applications in these environments.

The Dutch Wadden Sea (Figure 1) is an example of a complex coastal system that poses significant challenges to nearshore wave modeling. The region is enclosed by a series of barrier islands and the mainland coasts of the provinces of Friesland and Groningen. Tidal inlets are found between the barrier islands, each featuring an ebb tidal delta, one or more main tidal channels, and a complex system of smaller channels and flats extending into the Wadden Sea interior. Apart from the tidal channels, the Wadden Sea interior is shallow and flat, with tidally-modulated depths normally ranging between 0 m (dry fall) and 3 m.

The Amelander Zeegat tidal inlet (Figure 2) is found between the barrier islands of Terschelling (to the west) and Ameland (to the east). A program of wave monitoring has been operational in this inlet since 2003 [*Zijderveld and Peters* 2008]. Hindcast studies with SWAN based on this data [*Groeneweg et al.* 2008; *Van Vledder et al.* 2008] have shown the significant influence of currents on the prediction of wave fields in this tidal inlet. In following current, observations are typically well reproduced, but under strong opposing (near-blocking) current, wave heights are significantly overestimated. This affects the reliability with which these predictions can be applied in the assessment of safety against flooding, or other geophysical applications in such regions. This issue is addressed in the present study.

The influence of currents on wave fields are typically divided into effects on the wave kinematics and dynamics [*Johnsson* 1990]. The effects of currents on wave kinematics include effects on the wave phase velocity and the wave number and wavelength. Hence, waves traveling over a horizontally sheared current field experience current-induced refraction [e.g. *Zhang et al.* 2009]. The effect of currents on the wave dynamics can be derived from the energy or action balance equations. Waves propagating into an opposing current gradient with increasing strength will experience an increase in wave height; conversely, a following current gradient results in a reduction in wave height. When a wave field meets an opposing current with a velocity that approaches the wave group velocity, waves are blocked, which may cause steepness-induced breaking and reflection.

When currents interact with waves that are actively forced by wind, additional effects are found [*Haus* 2007]. Wind moving over a wave field in ambient opposing current will have a higher speed relative to the waves (a lower effective wave age) than without it, and a lower relative speed in the case of following current, even if the current field is spatially uniform. The result is a respective increase and decrease in the growth rate of the waves. In addition, *Haus* [2007] shows that wind-driven waves that experience current refraction over a horizontally sheared current can experience a reduction in their growth rate due to a shifting of the (wave-induced) wind stress away from the mean wind direction.

These kinematic, dynamic and wind-growth-related effects of currents are, in principle, included in the kinematic and dynamical equations of SWAN. The exception is the dissipative process that accompanies partial or full wave blocking. *Ris and Holthuijsen* [1996], hereafter RH96, show that SWAN, using the whitecapping expression of *Komen et al.* [1984], underestimates wave dissipation in such situations, leading to a strong overestimation in the significant wave height. Models for enhanced wave dissipation on opposing current have been proposed by RH96, *Chawla and Kirby* [1998, 2002] and *Suastika* [2004]. These authors all assume a bore-based breaker model (either *Battjes and Janssen* [1978] or *Thornton and Guza* [1983]) to be appropriate for modeling the dissipation, using the mean wave steepness as governing parameter. However, *Chawla and Kirby* [1998] note, from experimental observation, that current-induced breaking is very different from depth-induced breaking—the breaking is weak and unsaturated, as opposed to the saturated breakers observed in depth-induced breaking. As a practical problem, *Ris* [1997] reports that the model of RH96 fails under wind-wave growth situations, since young wind waves, being inherently steep, are too strongly dissipated. This approach is therefore unsuitable for field situations that feature a combination of wind growth and current interaction, such as the Dutch Wadden Sea. Hence an alternative approach for the dissipation modeling is required.

The present study aims to develop a formulation for the dissipation of waves on opposing current that is suitable for both mature waves and young wind sea, to calibrate it and to assess its performance for a range of laboratory and field situations.

Chawla and Kirby [1998] and *Suastika* [2004] report experimental observations that an originally monochromatic wave field develops a strong groupiness in the opposing current, and that waves tend to break at the crests of these wave groups. Such groupiness develops due to Benjamin-Feir instability in the steepening wave field, caused by the opposing current, leading to side band instabilities. A dissipation expression based on the groupiness of the waves has been proposed by *Alves and Banner* [2003]. Prompted by an apparent link between deep water wave breaking and wave groups [e.g. *Donelan et* *al.* 1972; *Holthuijsen and Herbers* 1986], *Banner et al.* [2000] demonstrate that the mean steepness of dominant waves (integrated over a bandwidth around the spectral peak) is well-correlated with their breaking probability, leading them to propose this quantity as the primary variable determining the breaking of dominant waves. *Banner et al.* [2002] extended the study of *Banner et al.* [2000] to spectral intervals above the spectral peak frequency, and replaced the mean steepness parameter by the spectral saturation as measure of the local spectral steepness. *Alves and Banner* [2003] incorporate these findings into a dissipation expression that features a primary dependence on the (frequency-local) spectral saturation. It is noted that some reservations have been stated concerning the causal link between dominant wave steepness, wave groups and the breaking probability [*Bababin and Van der Westhuysen* 2008]. However, considering the observations of *Chawla and Kirby* [1998], the relation between wave groups and breaking appears to be particularly strong in the case of current-induced wave steepening.

In the present study, the application of a saturation-based expression for the steepness dissipation of waves on opposing current is investigated. A number of saturation-based expressions have been proposed in the literature, including *Alves and Banner* [2003], *Young and Babanin* [2006] and *Ardhuin et al.* [2009]. In the present study, the expression of *Alves and Banner* [2003], as adapted by *Van der Westhuysen* [2007], is applied. It will be shown that the proposed calibration settings for this expression, obtained for wind wave growth conditions, yield too little dissipation on opposing current (as was found for the *Komen et al.* [1984] expression by RH96 and *Chawla and Kirby* [2002]). It is, however, conversely not desirable to recalibrate the whitecapping expression to levels sufficient for current-induced steepening at the expense of predictions for wind wave growth. Hence, a recalibration is proposed that yields enhanced dissipation proportional to degree of steepening of the wave field due to the opposing current. The latter is estimated from the propagation velocity in frequency space c_σ, normalized by the local radian frequency.

In order to investigate the different models for current-induced dissipation, a data set of 31 cases was assembled. These cases include the flume experiments of *Lai et al.* [1989], *Suastika* [2004] and field cases in the Amelander Zeegat during various storms. The data from the two flume experiments, plus field observations in the Amelander Zeegat during two NW storms, are used to calibrate the proposed formulation for enhanced dissipation on opposing current. The calibrated expression is subsequently validated for deep water, fetch-limited wave growth conditions in the absence of current (showing no influence, as expected), and field observations in the Amelander Zeegat during three more W and NW storms.

This paper is structured as follows: Section 2 presents the methodology followed in this study, including a description of the proposed enhanced dissipation expression. Section 3 presents the calibration of this expression, followed by a validation in Section 4. Section 5 closes the paper with conclusions.

2. Method

This section presents the methodology of this study. This includes a description of the additions to the action balance equation in SWAN (Section 2.1), the formulations for enhanced current-induced dissipation investigated (Section 2.2), the model settings applied (Section 2.3), the selection of calibration and validation cases (Section 2.4) and the statistical measures used to assess the model performance (Section 2.5).

2.1. Additions to the action balance equation

The spectral wind wave model SWAN computes the evolution of wave action density N ($= E/\sigma$, where E is the variance density and σ the relative radian frequency) using the action balance equation:

$$\frac{\partial N}{\partial t} + \nabla_{\mathrm{x,y}} \cdot \left[\left(\vec{c_{\mathrm{g}}} + \vec{U} \right) N \right] + \frac{\partial}{\partial \theta} \left(c_\theta N \right) + \frac{\partial}{\partial \sigma} \left(c_\sigma N \right) = \frac{S_{\mathrm{tot}}}{\sigma} \tag{1}$$

with

$$S_{\mathrm{tot}} = S_{\mathrm{in}} + S_{\mathrm{wc}} + S_{\mathrm{nl4}} + S_{\mathrm{bot}} + S_{\mathrm{brk}} + S_{\mathrm{nl3}} + \left(S_{\mathrm{wc,cur}} + S_{\mathrm{bot,perf}} \right) \tag{2}$$

The terms on the left-hand side of (1) represent, respectively, the change of wave action in time, the propagation of wave action in geographical space (with $\vec{c_{\mathrm{g}}}$ the wave group velocity vector and $\vec{U}$ the ambient current), depth- and current-induced refraction (with propagation velocity c_θ in directional space θ) and the shifting of the relative radian frequency σ due to variations in mean current and depth (with the propagation velocity c_σ). The right-hand side of (1) represents processes that generate, dissipate or redistribute wave energy, given by (2). In deep water, three source terms are dominant: the transfer of energy from the wind to the waves, S_{in}; the dissipation of wave energy due to whitecapping, S_{wc}; and the nonlinear transfer of wave energy due to quadruplet (four-wave) interaction, S_{nl4}. In shallow water, dissipation due to bottom friction, S_{bot}, depth-induced breaking, S_{brk}, and nonlinear triad (three-wave) interaction, S_{nl3}, are additionally accounted for.

In the present study, two additional source terms are included in (2). These are a term for the enhanced breaking dissipation of waves on a current $S_{\mathrm{wc,cur}}$, the subject of this study, and a special dissipation term $S_{\mathrm{bot,perf}}$ required for the evaluation of the *Suastika* [2004] laboratory data set (see Section 2.4.2 below).

2.2. Models for enhanced breaking dissipation on opposing current

Below, various formulations for steepness breaking (whitecapping) are presented. First, the saturation-based whitecapping expression proposed by *Van der Westhuysen* [2007] is presented. Subsequently, two formulations for enhanced breaking dissipation on opposing current are described, namely the expression of RH96 and the formulation proposed in the present study.

2.2.1. Saturation-based whitecapping

Van der Westhuysen [2007] proposes an adapted version of the saturation-based whitecapping formulation developed by *Alves and Banner* [2003]. This expression is combined with the wind input formulation proposed by *Yan* [1987]. The whitecapping expression of *Van der Westhuysen* [2007] is composed of two parts, namely a contribution to the dissipation by wave breaking, and a weaker non-breaking contribution:

$$S_{\mathrm{wc,SB}}(\sigma,\theta) = f_{\mathrm{br}}(\sigma) S_{\mathrm{dis,break}} + \left[1 - f_{\mathrm{br}}(\sigma)\right] S_{\mathrm{dis,non-break}} \quad , \tag{3}$$

where the breaking part is based on the saturation-based expression of *Alves and Banner* [2003], as modified by *Van der Westhuysen et al.* [2007]:

$$S_{\mathrm{dis,break}} = -C'_{\mathrm{ds}} \left[\frac{B(k)}{B_{\mathrm{r}}}\right]^{\frac{p}{2}} \left[\tanh(kd)\right]^{\frac{2-p}{4}} g^{\frac{1}{2}} k^{\frac{1}{2}} E(\sigma,\theta) \quad , \tag{4}$$

and the non-breaking part is based on the pulse-based expression of *Komen et al.* [1984]:

$$S_{\mathrm{dis,non-break}} = -C_{\mathrm{ds}} \left(\frac{k}{\tilde{k}}\right)^q \left(\frac{\tilde{s}}{\tilde{s}_{\mathrm{PM}}}\right)^r \tilde{\sigma} E(\sigma,\theta) \quad . \tag{5}$$

The weighting factor f_{br} determines the changeover from the dissipation of breaking to non-breaking waves. This weighting is a function of the ratio between the spectral saturation $B(k)$ and a threshold saturation level B_{r}:

$$f_{\mathrm{br}}(\sigma) = \frac{1}{2} + \frac{1}{2}\tanh\left\langle 10\left(\left[\frac{B(k)}{B_{\mathrm{r}}}\right]^{\frac{1}{2}} - 1\right)\right\rangle \tag{6}$$

For the spatial scales considered in the field cases of the present study, only the component (4) in the expression (3) is relevant. The parameter p is a function of the inverse wave age u_*/c, based on scaling arguments involving a spectral balance between the wind input, whitecapping and nonlinear interaction terms (see *Van der Westhuysen et al.* [2007] for details):

$$p\,(u_*/c) = 3 + \tanh\left[25\left(\frac{u_*}{c} - 0.1\right)\right] \tag{7}$$

In *Van der Westhuysen* [2007] the remaining parameters of (4) were calibrated to $C_{\mathrm{ds}} = 5.0 \times 10^{-5}$ and $B_{\mathrm{r}} = 1.75 \times 10^{-3}$ respectively.

2.2.2. Ris and Holthuijsen [1996]

As discussed in Section 1, RH96 show that the default, pulse-based whitecapping expression of *Komen et al.* [1984] does not provide sufficient wave breaking dissipation in situations of strong opposing current. They demonstrate that the addition of a dissipation term based on the bore-based breaker model of *Battjes and Janssen* [1978] to (2) is effective in the modeling of the rapid dissipation occurring near the blocking point. This expression reads:

$$S_{\mathrm{wc,cur}}(\sigma,\theta) = -C''_{\mathrm{ds}} Q_b \left(\frac{s_{\max}}{\tilde{s}}\right)^2 \tilde{\sigma} \frac{k}{\tilde{k}} E(\sigma,\theta) \quad , \tag{8}$$

where $\tilde{s} = \tilde{k}\sqrt{E_{tot}}$ is the mean wave steepness, $\tilde{\sigma}$ the mean relative radian frequency, given by

$$\tilde{\sigma} = E_{\mathrm{tot}}^{-1} \int_0^{2\pi} \int_0^{\infty} \sigma E(\sigma,\theta) d\sigma d\theta \tag{9}$$

and $\tilde{k}$ the mean wave number, defined as

$$\tilde{k} = \left(E_{\mathrm{tot}}^{-1} \int_0^{2\pi} \int_0^{\infty} \frac{1}{\sqrt{k}} E(\sigma,\theta) d\sigma d\theta \right)^{-2} \quad . \tag{10}$$

The proportionality coefficient $C''_{\mathrm{ds}} \equiv \alpha_{\mathrm{BJ}} = 1$. The variable Q_b is the fraction of breaking waves, determined by

$$\frac{1 - Q_b}{\ln Q_b} = -8 \frac{E_{\mathrm{tot}}}{H_m^2} \tag{11}$$

in which a maximum wave height H_m is defined based on a limiting steepness

$$H_m = \frac{2\pi s_{\max}}{\tilde{k}} \tag{12}$$

The limiting steepness $s_{\max}$ is set to 0.14, based on Miche's criterion for the limiting steepness of an individual breaker. We note that *Chawla and Kirby* [1998] show that when propagating on an opposing current, waves can break at a lower steepness than this. RH96 demonstrate that expression (8) enhances the dissipation for waves exceeding a mean steepness of $\tilde{s} = 0.08$, such as can occur in strong opposing current.

2.2.3. Enhanced saturation-based dissipation

Chawla and Kirby [2002] show that, as an alternative to the bore-based expression proposed by RH96, wave dissipation in opposing current can be modelled using a conventional whitecapping expression of the form (5), with an enhanced proportionality coefficient C_{ds}. As described in Section 1, experimental observations suggest that a saturation-based expression is appropriate for modeling current-induced breaking dissipation. Consequently, the basic form of the saturation-based (4) is applied here to model the enhanced dissipation due to wave-current interaction, given by $S_{\mathrm{wc,cur}}$ in (2). In order to isolate the contribution of currents, the degree of enhanced dissipation by (4) is scaled with the relative increase in steepness due to the opposing current, given by $\Delta s/s$. Dimensional analysis then yields:

$$S_{\mathrm{wc,cur}}(\sigma,\theta) = -C''_{\mathrm{ds}} \frac{\triangle s(\sigma,\theta)}{s(\sigma,\theta)} \left[\frac{B(k)}{B_{\mathrm{r}}}\right]^{\frac{p}{2}} E(\sigma,\theta) \quad . \tag{13}$$

For simplicity, deep water conditions are assumed, so that the shallow water scaling factor $[\tanh(kd)]^{\frac{2-p}{4}}$ in (4) is dropped. The current-induced increase in wave steepness is given by:

$$\triangle s = \frac{\partial s}{\partial t} = \frac{\partial}{\partial t}\left(\frac{H}{L}\right) = \frac{1}{L}\frac{\partial H}{\partial t} + H\frac{\partial}{\partial t}\left(\frac{1}{L}\right) \quad , \tag{14}$$

In which L and H are the wave length and a representative wave height at the spectral component (σ,θ). Normalizing by $s = H/L$ gives:

$$\frac{\triangle s}{s} = \frac{\partial H}{\partial t}/H + \frac{\partial L^{-1}}{\partial t}/L^{-1} \quad . \tag{15}$$

The deep water wave length at the radian frequency σ is given by:

$$L = 2\pi g \sigma^{-2} \quad , \tag{16}$$

and the wave height by a condition of constant action flux:

$$\left(\vec{c_{\mathrm{g}}} + \vec{U}\right) \frac{E(\sigma, \theta)}{\sigma} = F_{\mathrm{const}} \quad , \tag{17}$$

where F_{const} is the constant flux, so that

$$H \propto \left[\delta\sigma F_{\mathrm{const}} \sigma \left(\vec{c_{\mathrm{g}}} + \vec{U}\right)^{-1}\right]^{\frac{1}{2}} \quad . \tag{18}$$

where $\delta\sigma$ is a fixed small frequency increment. Assuming now that away from the actual blocking point $|\vec{c_{\mathrm{g}}}| \gg \left|\vec{U}\right|$, deep water conditions give:

$$H \propto \left[\frac{2}{g} \delta\sigma F_{\mathrm{const}} \sigma^2\right]^{\frac{1}{2}} \quad . \tag{19}$$

Substituting (16) and (19) in (15) yields:

$$\frac{\triangle s}{s} = \frac{\partial \sigma}{\partial t}/\sigma + \frac{\partial \sigma^2}{\partial t}/\sigma^2 = 3\frac{\partial \sigma}{\partial t}/\sigma \quad . \tag{20}$$

The change in the relative radian frequency in time due to interaction with current (and time-varying bathymetry) is given by $c_\sigma = \partial\sigma/\partial t$. Therefore, the change in steepness per (σ, θ) component due to the influence of current is given by:

$$\frac{\triangle s(\sigma,\theta)}{s(\sigma,\theta)} = 3\frac{c_\sigma(\sigma,\theta)}{\sigma} \quad . \tag{21}$$

Substituting (21) in (13) yields the source term:

$$S_{\mathrm{wc,cur}}(\sigma,\theta) = -C''_{\mathrm{ds}} \max\left[\frac{c_\sigma(\sigma,\theta)}{\sigma}, 0\right]\left[\frac{B(k)}{B_{\mathrm{r}}}\right]^{\frac{p}{2}} E(\sigma,\theta) \quad . \tag{22}$$

The enhanced dissipation is not required in situations of following current, where the elongated waves do not experience increased breaking. This is achieved with the maximum function, so that only frequency upshifts are taken into account. In the absence of direct observations, the parameterizations of B_{r} and p are taken similar to those of (4). Hence, (22) contains one additional calibration parameter relative to (4), namely the proportionality coefficient C''_{ds}. The calibration of this parameter is considered in Section 3.

2.3. Model settings

The computations presented here were performed using the SWAN model version 40.72ABC, in stationary third-generation mode. For the deep water physics, the combination of wind input S_{in} and saturation-based whitecapping S_{wc} of *Van der Westhuysen* [2007], presented in Section 2.2.1, was applied. Quadruplet nonlinear interaction S_{nl4} was modelled using the Discrete Interaction Approximation (DIA) of *Hasselmann et al.* [1985]. The shallow water source terms include triad nonlinear interaction S_{nl3} according to *Eldeberky* [1996] and bottom friction according to *Hasselmann et al.* [1973], both with their default settings in SWAN. For depth-induced breaking S_{brk}, the biphase breaker model of *Van der Westhuysen* [2010] was applied, with the extension proposed by *Van der Westhuysen* [2009]. In the Amelander Zeegat field cases, wave diffraction, which may redistribute the energy of waves steepened by the current, is taken into account with the phase-decoupled diffraction expression of *Holthuijsen et al.* [2003]. Hereafter, these settings will be referred to as the default model. Two further variants are studied, featuring the additional expressions for enhanced current-induced dissipation of RH96 given by (8) and the proposed expression (22). The convergence criteria applied are the so-called curvature-based criteria proposed by *Zijlema and Van der Westhuysen* [2005].

2.4. Data sets

In order to assess the performance of the proposed expression for wave dissipation on opposing current, a data set of laboratory and field cases have been assembled. These are presented below.

2.4.1. Lai et al. [1989] flume experiment

Lai et al. [1989] investigated the transformation of the wave spectrum under strong opposing current in a flume of 8 m length and 0.75 m depth. A current flow was induced along the flume, which was contracted by the presence of a shoal, resulting in an increase in the current velocity from U = -0.13 to -0.22 m/s. Random, long-crested waves were mechanically generated at the downstream end of the flume. In the case considered here, the incident wave field had a significant wave height of $H_{\mathrm{m0}} = 0.019$ m and a mean period of $T_{\mathrm{m01}} = 0.5$ s. This represents a partial blocking situation with $U/c_{\mathrm{g,peak}} = 0.52$, which resulted in a strong reduction in the observed significant wave height over the shoal, in combination with an increase in the absolute mean wave period T_{m01}.

2.4.2. Suastika [2004] flume experiment

Suastika et al. [2000] and *Suastika* [2004] studied partial and full wave blocking using a 35 m long flume, with a 12 m measurement section at its center. Three of these cases are considered here, all involving partial blocking with $U/c_{\mathrm{g,peak}} = 0.47$ (Table 1). Random waves (JONSWAP spectrum) were mechanically generated at the one end of the flume, while a water head difference induced an opposing current flow along the flume. At the measurement section, the flow was contracted by a false wall and perforated bottom to create a sump for suction pumps. Here water was gradually withdrawn through the bottom of the flume, creating an opposing current that reduced approximately linearly to zero in the up-wave direction. However, the presence of this perforated false bottom had the disadvantage of introducing an additional source of dissipation, that must be added to (2). The dissipation due to the interaction between the waves and the false bottom is given by:

$$S_{\mathrm{bot,perf}}(\sigma, \theta) = 2\mu_b c_g E(\sigma, \theta) \tag{23}$$

where μ_b is a coefficient that is dependent on the wave height and period, which was empirically estimated by *Suastika* [2004]. This source of dissipation, which is significant, is accounted for in the simulations for this experiment, but is irrelevant for general application.

2.4.3. Amelander Zeegat

Conditions in the Dutch Wadden Sea are represented by a collection of 27 stationary cases taken from NW and W storms occurring over the Amelander Zeegat during 2007. The NW storms feature high water levels (up to 2.6 m NAP) combined with wind speeds of up to 18.5 m/s from 320-331°N (Table 2), whereas the W storms feature wind speeds of up to 20.3 m/s from 264-279°N (Table 3). During the NW events, the wind and offshore waves are directed more or less straight into the tidal channel. Although during W events the wind direction was not parallel to the tidal channel, offshore waves propagate into the tidal inlet by refraction over the ebb tidal delta. During these events, two arrays of wave buoys were placed along transects through the tidal inlet (Figure 2). The buoys AZB32, AZB42 and AZB52 in the main channel were well-situated to record conditions of wave-current interaction. Currents were not measured, but computed using the hydrodynamic model Delft3D including tidal, wind and wave forcing, calibrated to water level observations

2.5. Method of analysis

The predictive ability of the dissipation expressions (8) and (22) was determined on the basis of scatter index and relative bias scores, which were computed for both the significant wave height H_{m0} and the mean period $T_{\mathrm{m-1,0}}$. These measures are defined respectively as

$$\text{Rel. bias}_{\Psi} = \frac{\sum_{i=1}^{N} (\Psi^{i}_{\mathrm{SWAN}} - \Psi^{i}_{\mathrm{obs}})}{\sum_{i=1}^{N} \Psi^{i}_{\mathrm{obs}}} \quad , \tag{24}$$

and

$$\mathrm{SI}_{\Psi} = \frac{\sqrt{\frac{1}{N}\sum_{i=1}^{N}\left(\Psi_{\mathrm{SWAN}}^{i} - \Psi_{\mathrm{obs}}^{i}\right)^2}}{\frac{1}{N}\sum_{i=1}^{N}\Psi_{\mathrm{obs}}^{i}} \tag{25}$$

where Ψ_{obs} is the observed significant wave height $H_{\mathrm{m0,obs}}$ or mean period $T_{\mathrm{m-1,0,obs}}$, and Ψ_{SWAN} is the corresponding modelled value $H_{\mathrm{m0,SWAN}}$ or $T_{\mathrm{m-1,0,SWAN}}$, in a sample of size N. These statistical measures were computed over all cases for a given laboratory or field situation (e.g., *Suastika* [2004] or Amelander Zeegat). Subsequently, these individual scores were combined with a weighted average (based on the number of cases per situation) to obtain overall scores for, for example, the total validation subset.

For the calibration of the dissipation model, a third statistical measure was used, namely a combined error function ε. This error function is defined in terms of the scatter indices of H_{m0} and $T_{\mathrm{m-1,0}}$, as follows:

$$\varepsilon = \frac{1}{2}\left(SI_{\mathrm{H}} + SI_{\mathrm{T}}\right) \tag{26}$$

using the definition in (25). As above, this error function was computed over all cases for a given laboratory or field situation. By considering the weighted mean of the error ε over a collection of cases, optimal calibration settings were determined for the total calibration subset.

3. Calibration

The expression for enhanced dissipation (4) features one calibration parameter, namely the proportionality coefficient C''_{ds}, the calibration of which is considered in this section. Before this calibration is carried out, however, the impact of additional processes relevant to the flume cases of *Suastika* [2004] is investigated. These include amplitude dispersion and dissipation due to the perforated false bottom of the flume.

3.1. Amplitude dispersion and dissipation by percolation

As described in Section 2.4.2, the experimental setup of *Suastika* [2004] featured a perforated false bottom, which introduced an additional source of dissipation that should be taken into account in the model. The dissipation due to the perforated false bottom is given by (23), not included in the standard version of SWAN. In addition, amplitude dispersion can be important in predicting wave evolution and the location of the blocking point for fully-blocking cases [*Chawla and Kirby* 2002]. Although the latter is less relevant for the partial blocking situations investigated here, the influence of both these processes is assessed first before considering the calibration of (22). When only applying dissipation by the whitecapping expression of *Van der Westhuysen* [2007], the significant wave height is strongly overestimated along most of the flume (Figure 3). Accounting for dissipation due to the perforated false bottom (23) reduces the overestimation in wave height by about half. Since this process significantly influences the results, it is included in the *Suastika* [2004] cases in the calibration below (Section 3.2). The effects of higher-order dispersion can be included rigorously in spectral wave models such as SWAN by using the expression of *Willebrand* [1975]. Here the effects are approximated, to assess their influence. This is done by including Stokes third-order dispersion in the wave propagation [e.g. *Kirby and Dalrymple* 1986]:

$$\sigma^2 = gk\left(1+\epsilon^2 D\right)\tanh(kd) \tag{27}$$

where

$$D = \frac{\cosh(4kd) + 8 - 2\tanh^2(kd)}{8\sinh^4(kd)} \quad . \tag{28}$$

The wave steepness at each spectral component is given by $\epsilon = k|A|$, in which $|A|$ is a characteristic wave amplitude, taken here as $|A| = H_{rms}/2$.

Applying (27) and (28) to the partial blocking laboratory flume cases has only a modest influence on the wave evolution along the flume (e.g. Figure 3). The addition of higher-order dispersion therefore does not appear to correct the overestimation of significant wave heights in the opposing current. In the Amelander Zeegat tidal inlet, less severe wave-current interaction is found, and hence the effect of higher order dispersion is expected to be even less. As a result, higher-order dispersion was not taken into account in the remainder of this study.

3.2. Calibration of enhanced dissipation term

The laboratory flume case of *Lai et al.* [1989] and the partial blocking cases of *Suastika* [2004] were used for the calibration of (22). Figure 4 presents the calibration of C''_{ds} by means of the optimalization of the error function ε, where SI_{H} and SI_{T} are the scatter indices of H_{m0} and $T_{\mathrm{m-1,0}}$ respectively. Panels (b) and (c) show that in the individual calibration subsets of *Lai et al.* [1989] and *Suastika* [2004] the error ε has a local maximum at $C''_{\mathrm{ds}} = 0$ and a strong reduction over $0 < C''_{\mathrm{ds}} < 0.5$, indicating the importance of including the dissipation term (22). The calibration result for the total calibration data set (panel (a)) gives an optimal setting of $C''_{\mathrm{ds}} = 0.65$.

Figure 5 presents the calibration results with $C''_{\rm ds} = 0.65$ along the flume for two of the laboratory cases, with the results for the RH96 expression included for comparison. The left-hand panels of Figure 5 show the calibration results for a partial blocking case of *Suastika* [2004]. A significant improvement in the H_{m0} results is found over that of both the default and RH96. The mean wave period is predicted less accurately, however, showing an overestimation approaching the partial blocking point. Examination of the frequency spectra reveals that this is due to an exaggerated frequency-downshift of spectral components in SWAN (not shown). For the flume case of *Lai et al.* [1989], the strong overestimation of significant wave height with the default model is corrected using (22) (Figure 5, right-hand panel). This improvement is similar to that found with the RH96 expression.

4. Validation

In this section, the performance of the calibrated expression (22) is evaluated on the basis of the validation data set, and compared with the performance of the RH96 expression. The model performance is first assessed for idealised fetch-limited wave growth without current. This is done in order to verify the desired characteristic that the expression for enhanced current-induced dissipation should not affect model results in the absence of ambient current. Subsequently, the proposed expression is validated for the complex field situation of the Amelander Zeegat.

4.1. Idealized fetch-limited wave growth

Figure 6 presents simulation results for deep water fetch-limited wave growth, for a wind speed of $U_{10} = 20$ m/s. The results of three model variants are shown, namely (i) the default model featuring the whitecapping expression of *Van der Westhuysen* [2007], (ii) the default model with the addition of the enhanced dissipation (22), and (iii) the default model with the addition of the enhanced dissipation proposed by RH96. First, as expected, Figure 6 shows that the default model produces a satisfactory growth curve through the observations of *Kahma and Calkoen* [1992]. Second, on this scale, the results of the model variant including (22) cannot be distinguished from the default model. This verifies the desired characteristic that the expression for enhanced current-induced dissipation should not affect wave growth results in the absence of ambient current, as is also apparent from inspection of (22).

By contrast, Figure 6 shows that the application of the RH96 expression to the default model yields a strong underestimation wave growth for younger wind sea, up to a fetch of about $X^* = 1 \times 10^6$. This result is analogous to that presented by *Ris* [1997], who used *Komen et al.* [1984] whitecapping as basis. *Ris* [1997] argued that this spurious model performance is due to excessive dissipation of steep young waves by the RH96 expression. The length scales over which this underestimation of wave growth occurs are relevant for the Wadden Sea situation, in particular for local wind sea growth in the Wadden Sea interior, as will be shown below.

4.2. Amelander Zeegat validation subset

The model performance is subsequently considered for the validation subset featuring NW and W storms recorded in the Amelander Zeegat inlet in 2007. The conditions in these cases are equally distributed between opposing and following current in the inlet, with a number of opposing current cases exceeding 1 m/s. Scaled with the wave group velocity, maximum opposing relative current speeds of around $U/c_{g,peak} = 0.4$ are found, which is still relatively far from the blocking point. Figure 7 compares model results with observations in terms of scatter plots of H_{m0}, $T_{\mathrm{m-1,0}}$ and the non-dimensional ratio H_{m0}/d. These parameters have been computed for the frequency range 0.03-0.5 Hz. The left-hand column presents the results of the default model, featuring the whitecapping expression of *Van der Westhuysen* [2007]. Although the general agreement between the model results and the observations is good, the wave heights in the tidal channel (buoys AZB32/42/52, filled symbols, with statistics given in parentheses) are overestimated by an average of 9%. For conditions with opposing current, this is related to insufficient dissipation of waves steepening in opposing current, as illustrated by the flume cases above. The results for the mean period and the H_{m0}/d ratio show good agreement with the observations, albeit with some overestimation at higher periods and a slight negative bias in higher values of H_{m0}/d (middle and bottom left-hand panels). The center column of Figure 7 presents the simulation results of the default model including the additional expression of RH96. With this additional term, the overestimation of the significant wave height at the buoys AZB32/42/52 in the channel is reduced to 4%. However, the integral parameters at the buoys in the shallow interior (AZB41/51/61/62) are now structurally underpredicted. This is seen, for example, in the underprediction of the higher values of H_{m0}/d, which are associated with this region (bottom panels). For these buoys, steep, young wind sea is excessively dissipated by RH96, as was found in the fetch-limited growth curve results in Figure 6 above. As a result, the overall statistics of this model variant are poorer than those of the default model.

The right-hand column of Figure 7 presents the corresponding results for the default model in combination with the enhanced dissipation (22), using the calibrated value $C''_{\mathrm{ds}} =$

0.65. For the channel buoys AZB32/42/52, the 9% overestimation in H_{m0} found with the default model is now corrected (top panels). The improvement is the most pronounced for the cases of the November 2007 storm, for which a number of data points were overestimated using the default model. For the Jan/Mar 2007 storms, similar, although less pronounced, improvement in predicted significant wave heights is seen. However, importantly, application of (22) does lead to a significant deterioration in model results for younger wind sea over the tidal flats at the buoys AZB41/51/61/62, as is the case with the RH96 expression (compare bottom panels showing H_{m0}/d ratio). Note that the overall error statistics of both H_{m0} and H_{m0}/d show a greater negative bias with the inclusion of (22). This is because the remaining dissipation terms have been calibrated previously without taking the new expression into account, so that some double counting of dissipation may occur. Comparison between the panels in the center row shows that the results for the absolute mean period $T_{\mathrm{m}-1,0}$ improve somewhat with the application of (22).

Figure 8 shows examples of the frequency spectra at the wave buoys AZB42 in the tidal channel and AZB61 on the tidal flats, away from the tidal current, produced by the three model variants under ebb (opposing current) conditions. At AZB42, the default model significantly overestimates the wind sea growth in the opposing current, with an overestimation of both the total variance and the peak period. Application of the RH96 enhanced dissipation expression yields some improvement, but still overestimates the observed variance. By contrast, at the buoy AZB61, located on the tidal flats, the RH96 model significantly underestimates the growth of the young wind sea, as was seen in the scatter plots above. The model run featuring the enhanced whitecapping expression of (22) yields a better prediction at AZB42 than either the default or the RH96 variants, although the frequency downshift is still not corrected. Furthermore, unlike with the RH96 expression, the results at the remaining shallow water buoys are mostly unaffected, as desired.

Figure 9 shows examples of frequency spectra at AZB42 and ABZ61 under flood conditions (opposing current) in the inlet. For these cases the default model reproduces the observed spectra fairly well. Since waves are elongated under the influence of following current, characterized by a frequency downshift, the formulation (22) will not have any effect. Indeed, at the buoy location AZB42, the model results only have a small sensitivity to the application of either the RH96 or the proposed dissipation expressions, as desired. The exception is the case f102am07z011, for which some spectral directions experience opposing current, and are dissipated as a result. However, as seen above, the RH96 expression yields strong underestimations at the buoy AZB61 on the tidal flats. By contrast, the model variant featuring the enhanced dissipation (22) only has a limited impact on the results at these locations.

Figure 10 shows the spatial distribution of the effect of the proposed model on the integral parameters H_{m0} and mean period $T_{\mathrm{m}-1,0}$ for the presented ebb and flood cases. The top left-hand panel of Figure 10 shows that in the ebb case f102am07z009, the wave heights in the tidal channel diminish by up to 30% due to the enhanced dissipation of (22) under the opposing currents. The spatial pattern of the influence on the wave heights reflects that of a typical ebb current pattern, suggesting that only waves under opposing current are affected. By comparison, the mean period $T_{\mathrm{m}-1,0}$ experiences relatively little change due to the application of (22) (bottom left-hand panel). It is interesting to observe that in some parts of the tidal inlet the mean period increases due to the enhanced dissipation, like for example at AZB32. Inspection of the frequency spectra reveals this to be due to the reduction of the wind sea peak while the lower-frequency peak from the North Sea wave system remains intact (not shown).

The right-hand panels of Figure 10 show the spatial distribution of the impact of the proposed model (22) on H_{m0} and mean period $T_{\mathrm{m}-1,0}$ results for the flood case f102am07z006. The impact on the significant wave height is generally smaller than for the presented ebb case. This is particularly so in the main tidal channel at the buoys AZB32/42. However, as seen in the frequency spectra results above, the impact of the enhanced dissipation is not negligible everywhere. This is due to the fact that even under flood conditions the complex spatial current patterns over the channel system result in opposing current situations at some locations, resulting in additional dissipation according to (22). The bottom right-hand panel of Figure 10 shows the proposed model to have only a marginal impact on the mean period $T_{\mathrm{m}-1,0}$ results for this flood case.

5. Conclusions

The present study aimed to correct the overestimation of wave heights on opposing current in SWAN, as found in the tidal channels of the Wadden Sea. This model inaccuracy was addressed by means of the development of a formulation for the enhanced breaking dissipation of waves that is related to the degree of their current-induced steepening. This formulation was calibrated and validated for a range of laboratory and field situations. The following conclusions can be drawn from the results of this study:

1. Using a diverse set of laboratory and field cases, this study shows that when using conventional whitecapping expressions in SWAN, which are calibrated for wind wave

growth, significant wave heights are overestimated in the presence of opposing current. This confirms earlier results of *Ris and Holthuijsen* [1996].

2. The results of this study confirm that the addition of enhanced whitecapping dissipation according to *Ris and Holthuijsen* [1996] improves results for laboratory cases. However, as shown by *Ris* [1997], this expression leads to underestimation of young wind sea due to their inherent high steepness. This results in significant underestimation of locally-generated wind sea over the tidal flats in the Wadden Sea interior.

3. A new formulation for the enhanced dissipation of waves on opposing current is proposed, which is based on the saturation-based formulation of *Van der Westhuysen et al.* [2007], and scaled with the degree of current-induced steepening of the wave field. The latter is related to the current-induced Doppler shifting per spectral component. This expression contains one additional unknown parameter, which was calibrated to a value of $C''_{\mathrm{ds}} = 0.65$ using laboratory and field observations.

4. Validation of the proposed enhanced dissipation term for a data set of Amelander Zeegat field cases shows that the overestimation of significant wave heights at the channel buoys under opposing current is corrected. The satisfactory prediction of the mean period $T_{\mathrm{m}-1,0}$ is retained and somewhat improved. For situations with following current, no deterioration of results is found. In particular, the results for the locally-generated wind sea on the tidal flats are not significantly affected, unlike with the expression of *Ris and Holthuijsen* [1996].

5. Due to the complex tidal channel system and resulting current patterns in the Wadden Sea, local regions of opposing current (in the inlet and over the flats) may be found for flood conditions. At these locations, the enhanced breaking dissipation on opposing

current results in increased dissipation. Since in such regions the remaining dissipation terms in SWAN have been calibrated without this enhanced dissipation term, the addition of the proposed formulation results in some deterioration of the overall statistics.

Acknowledgments. The presented work is part of the SBW (Strength and Loads on Water Defenses) project commissioned by Rijkswaterstaat Centre for Water Management in the Netherlands. The Delft Universitiy of Technologiy is acknowledged for their kind permission to use the data set of *Suastika* [2004].

References

Alves, J. H. G. M., Banner, M. L. (2003), Performance of a saturation-based dissipation-rate source term in modelling the fetch-limited evolution of wind waves. J. of Phys. Oceanogr., 33, 1274–1298.

Ardhuin, F., W. E. Rogers, A. V. Babanin, J.-F. Filipot, R. Magne, A. Roland, A. J. van der Westhuysen, P. Queffeulou, J.-M. Lefevre, L. Aouf, and F. Collard (2010), Semi-empirical dissipation source functions for ocean waves: Part I, definitions, calibration and validations, J. Phys. Oceanogr., in press.

Babanin, A. V. and A. J. van der Westhuysen (2008), Physics of 'saturation-based' dissipation functions proposed for wave forecast models. J. Phys. Oceanogr., 38, 1831–1841

Banner, M. L., Babanin, A. V., Young, I. R. (2000), Breaking probability for dominant waves on the sea surface. J. of Phys. Oceanogr., 30, 3145–3160.

Banner, M. L., Gemmrich, J. R., Farmer, D. M. (2002), Multiscale measurements of ocean wave breaking probability. J. of Phys. Oceanogr., 32, 3364–3375.

Battjes, J. A., and J. P. F. M. Janssen (1978), Energy loss and set-up due to breaking of random waves, Proc. 16th Int. Conf. Coastal Eng., ASCE, 569–588.

Booij, N., R. C. Ris and L. H. Holthuijsen (1999), A third generation wave model for coastal regions, Part I, Model description and validation, J. Geophys. Res., 104, C4, 7649–7666.

Chawla, A. and J. T. Kirby (1998), Experimental study of wave breaking and blocking on opposing currents, , Proc. 26th Int. Conf. Coastal Eng., ASCE, 759–772.

Chawla, A. and J. T. Kirby (2002), Monochromatic and random wave breaking at blocking points, J. Geophys. Res., 107(C7), 10.1029/2001JC001042.

Donelan, M. A., Longuet-Higgins, M. S., Turner, J. S. (1972). Periodicity in whitecaps, Nature, 239, 449–451.

Eldeberky, Y. (1996), Nonlinear transformations of wave spectra in the nearshore zone, Ph.D Thesis, Fac. of Civil Engineering, Delft University of Technology, 203 pp.

Groeneweg, J., A. J. van der Westhuysen, G. P. van Vledder, S. Jacobse, J. Lansen and A.R. van Dongeren (2008), Wave modelling in a tidal inlet: Performance of SWAN in the Wadden Sea, Proc. 31th Int. Conf. Coastal Eng., ASCE, 411–423.

Haus, B. K. (2007), Surface current effects on the fetch-limited growth of wave energy, J. Geophys. Res., 112, C03003, doi:10.1029/2006JC003924.

Hasselmann, K., T. P. Barnett, E. Bouws, H. Carlson, D. E. Cartwright, K. Enke, J. A. Ewing, H. Gienapp, D. E. Hasselmann, P. Kruseman, A. Meerburg, O. Müller, D. J. Olbers, K. Richter, W. Sell, and H. Walden (1973), Measurement of windwave growth and swell decay during the Joint North Sea Wave Project (JONSWAP), Dtsch. Hydrogr. Z. Suppl., A(8), 12, 95 pp.

Hasselmann, S., K. Hasselmann, J. A. Allender, and T. P. Barnett (1985), Computations and parameterizations of the nonlinear energy transfer in a gravity-wave spectrum. Part 2: parameterization of the nonlinear transfer for application in wave models, J. of Phys. Oceanogr. 15, 1378–1391.

Holthuijsen, L. H., A. Herman and N. Booij (2003), Phase-decoupled refraction-diffraction for spectral wave models, Coastal Eng., 49, 291–305.

Holthuijsen, L. H. and Herbers, T. H. C. (1986), Statistics of breaking waves observed as whitecaps in the open ocean, J. of Phys. Oceanogr., 16, 290–297.

Johnsson, I. G. (1990), Wave-current interaction, in The Sea: Ocean Engineering Science, vol. 9B, edited by B. LeMéhauté and D. Hanes, pp. 65-120, John Wiley, Hoboken, N. J.

Kahma, K. K. and C. J. Calkoen (1992), Reconciling discrepancies in the observed growth of wind-generated waves, J. of Phys. Oceanogr., 22, 1389–1405.

Kirby, J. T. and R. A. Dalrymple (1986), An approximate model for nonlinear dispersion in monochromatic wave propagation models, Coastal Eng., 9, 545–561.

Komen, G. J., S. Hasselmann, and K. Hasselmann (1984), On the existance of a fully developed wind-sea spectrum, J. of Phys. Oceanogr. 14, 1271–1285.

Lai, R. J., S. R. Long and N. E. Huang (1989), Laboratory studies of wave-current interaction: Kinematics of the strong interaction, J. Geophys. Res., 94, 16,201–16,214.

Ris, R. C. (1997), Spectral modelling of wind waves in coastal waters, Ph.D Thesis, Fac. of Civil Eng., Delft Univ. of Tech., 160pp.

Ris, R. C., and L. H. Holthuijsen (1996), Spectral modelling of current wave-blocking. Proc. 25th Int. Conf. on Coastal Eng., ASCE, 1247–1254.

Suastika, I. K. (2004), Wave blocking, Ph.D Thesis, Fac. of Civil Eng., Delft Univ. of Tech., 157pp.

Suastika, I. K., M. P. C. de Jong and J. A. Battjes (2000), Experimental study of wave blocking, Proc. 27th Int. Conf. on Coastal Eng., ASCE, 227–240.

Thornton, E. B., and R. T. Guza (1983), Transformation of wave height distribution, J. Geophys. Res. 88, 5925–5938.

Van der Westhuysen, A. J. (2007), Advances in the spectral modelling of wind waves in the nearshore, Ph.D Thesis, Fac. of Civil Eng., Delft Univ. of Tech., 207pp.

Van der Westhuysen, A. J. (2009), Modelling of depth-induced wave breaking over sloping and horizontal beds, Proc. 11th Int. Workshop on Wave Hindcasting and Forecasting. *http://www.waveworkshop.org/11thWaves/Papers.*

Van der Westhuysen, A. J. (2010), Modelling of depth-induced wave breaking under finite-depth wave growth conditions, J. Geophys. Res, 115, C01008, doi:10.1029/2009JC005433.

Van der Westhuysen, A. J., M. Zijlema, and J. A. Battjes (2007), Nonlinear saturationbased whitecapping dissipation in SWAN for deep and shallow water, Coastal Eng., 54, 151–170.

Whitham, G. B. (1967), Non-linear dispersion of water waves, J. Fluid Mech., 27, 399–412.

Willebrand, J. (1975), Energy transport in a nonlinear and inhomogeneous random gravity wave field, J. Fluid Mech., 70, 113–126.

Van Vledder, G. P., J. Groeneweg and A. J. van der Westhuysen (2008), Numerical and physical aspects of wave modelling in a tidal inlet, Proc. 31th Int. Conf. Coastal Eng., ASCE, 424–436

Yan, L. (1987). An improved wind input source term for third generation ocean wave modelling. Technical Report No. 87-8, Royal Dutch Meteor. Inst. (KNMI).

Young, I. R. and Babanin, A. V. (2006), Spectral distribution of energy dissipation of wind-generated waves due to dominant wave breaking. J. Phys. Oceanogr., 36, 376–394.

Zhang, F. W., W. M. Drennan, B. K. Haus, and H. C. Graber (2009), On wind-wave-current interactions during the Shoaling Waves Experiment, J. Geophys. Res., 114, C01018, doi:10.1029/2008JC004998.

Zijderveld, A., and H. Peters (2008), Measurement programme Dutch Wadden Sea, Proc. 31th Int. Conf. Coastal Eng., ASCE, 404–410.

Zijlema, M., and A. J. van der Westhuysen (2005), On convergence behaviour and numerical accuracy in stationary SWAN simulations of nearshore wind wave spectra, Coastal Eng., 52, 237–256.

Figure 1. Bathymetry of the Dutch Wadden Sea in the north of the Netherlands, with depths in m below NAP (Dutch leveling datum). Rectangle indicates the location of the Amelander Zeegat region (detail in Figure 2). Projection in Dutch RD system.

Figure 2. Bathymetry of the Amelander Zeegat region in the Dutch Wadden Sea, including the location of the wave buoys (circles). Depth contours in m below NAP and projection in Dutch RD system.

Figure 3. Influence of perforated bottom dissipation (22) and amplitude dispersion (25) for case l100suast002 in the *Suastika* [2004] flume experiment. Shown are results without (22) and (25) (thin solid), with perforated bottom dissipation (22) (think solid), and with both (22) and (25) (dashed).

Figure 4. Calibration of (22). Error function ε as function of proportionality coefficient $C"_{\mathrm{ds}}$ for various calibration subsets.

Figure 5. Calibration results of (22) for case l100suast002 of the flume experiment of *Suastika* [2004] (left, including perforated bottom dissipation) and *Lai et al.* [1989] (right). Comparison between *Van der Westhuysen* [2007] (thin solid) whitecapping only, and with RH96 (dashed) and proposed model with $C"_{\mathrm{ds}} = 0.65$ (thick solid).

Figure 6. Fetch-limited wave growth curves for the *Van der Westhuysen* [2007] whitecapping (thin solid), and with additional enhanced whitecapping according to RH96 (dashed) and proposed expression (thick solid). Note that the latter is indistinguishable from the original *Van der Westhuysen* [2007] result at this scale. Observations of *Kahma and Calkoen* [1992] indicated by circles, with $X^* = gX/u_*^2$, $E^* = g^2E/u_*^4$ and $f_p^* = u_* f_p/g$.

Figure 7. Scatter plot results for the Amelander Zeegat validation cases. Comparison between *Van der Westhuysen* [2007] whitecapping only (left column), and with RH96 (center) and

proposed model with $C\text{"}_{\mathrm{ds}} = 0.65$ (right). Shown are results of Jan/Mar 2007 (inverted triangles) and Nov 2007 (circles). Buoys AZB32/42/52 in the tidal channel have filled symbols.

Figure 8. Frequency spectra results for four Amelander Zeegat stationary cases during ebb (refer Table 3). Results shown for the default (thin solid), RH96 (dashed) and proposed (thick solid) models. Observations indicated by line with circles.

Figure 9. Frequency spectra results for four Amelander Zeegat stationary cases during flood (refer Table 3). Results shown for the default (thin solid), RH96 (dashed) and proposed (thick solid) models. Observations indicated by line with circles.

Figure 10. Impact of proposed model (22) on spatial fields of wave parameters. Left-hand panels: Amelander Zeegat case f102am07z009 (ebb). Right-hand panels: Amelander Zeegat case f102am07z006 (flood).

Table 1. Selected cases from the laboratory flume experiment of *Suastika* [2004].

Case	Q (m^3/s)	H_{m0} (m)	T_p (s)
l100suast003	0.078	0.2	1.1
l100suast002	0.078	0.5	1.1
l100suast004	0.078	0.8	1.1

Table 2. Selected cases for the NW storms recorded during November 2007 in the Amelander Zeegat. Wind speed and direction are spatial averaged observations. Water levels at station AZB11. Current speed and direction are computed values at buoy location AZB42.

Case	Date and time (UTC)	U_{10} (m/s)	$U_{\rm dir}$ (°N)	WL (m NAP)	U (m/s)	θ_c (°Cart)
f102am07z016	08/11/2007 18:10	11.8	282	1.3	1.27	322
f102am07z017	09/11/2007 00:10	15.6	323	0.7	0.87	141
f102am07z018	09/11/2007 02:20	15.8	320	0.3	0.75	144
f102am07z019	09/11/2007 04:50	17.3	322	1.5	1.24	322
f102am07z020	09/11/2007 08:10	18.2	325	2.6	0.30	326
f102am07z021	09/11/2007 09:20	18.4	326	2.4	0.69	141
f102am07z022	09/11/2007 11:00	18.5	328	1.7	1.32	138
f102am07z023	09/11/2007 12:30	18.2	331	1.0	1.24	140
f102am07z024	09/11/2007 14:30	18.0	328	0.4	1.28	141
f102am07z025	09/11/2007 17:20	16.8	325	1.0	0.62	312
f102am07z026	09/11/2007 19:10	15.8	331	1.5	0.51	323
f102am07z027	09/11/2007 20:30	15.5	326	1.5	0.22	139

Table 3. Selected cases for the W storms recorded during January and March 2007 in the Amelander Zeegat. Wind speed and direction are spatial averaged observations. Water levels at station Nes. Current speed and direction are computed values at buoy location AZB42.

Case	Date and time (UTC)	U_{10} (m/s)	U_{dir} (°N)	WL (m NAP)	U (m/s)	θ_c (°Cart)
f102am07z028	11/01/2007 04:00	11.9	237	1.36	1.39	140
f102am07z032	11/01/2007 16:00	14.8	265	1.06	0.58	137
f102am07z033	11/01/2007 16:40	14.8	264	0.95	0.78	140
f102am07z034	11/01/2007 20:40	18.2	268	0.44	0.60	141
f102am07z003	11/01/2007 22:40	18.8	279	1.29	0.44	325
f102am07z006	18/01/2007 17:20	20.3	267	1.43	0.69	326
f102am07z039	18/01/2007 18:00	20.1	268	1.82	0.54	323
f102am07z040	18/01/2007 18:40	19.9	269	2.24	0.29	331
f102am07z042	19/01/2007 07:40	13.1	271	1.45	0.74	323
f102am07z043	19/01/2007 12:00	14.3	272	1.36	1.36	139
f102am07z044	18/03/2007 07:40	14.8	274	1.10	1.03	323
f102am07z045	18/03/2007 09:20	13.8	275	1.76	0.49	324
f102am07z009	18/03/2007 14:40	18.1	266	0.67	1.16	140
f102am07z010	18/03/2007 15:40	17.9	271	0.63	0.83	141
f102am07z011	18/03/2007 17:00	17.1	268	1.17	1.00	324

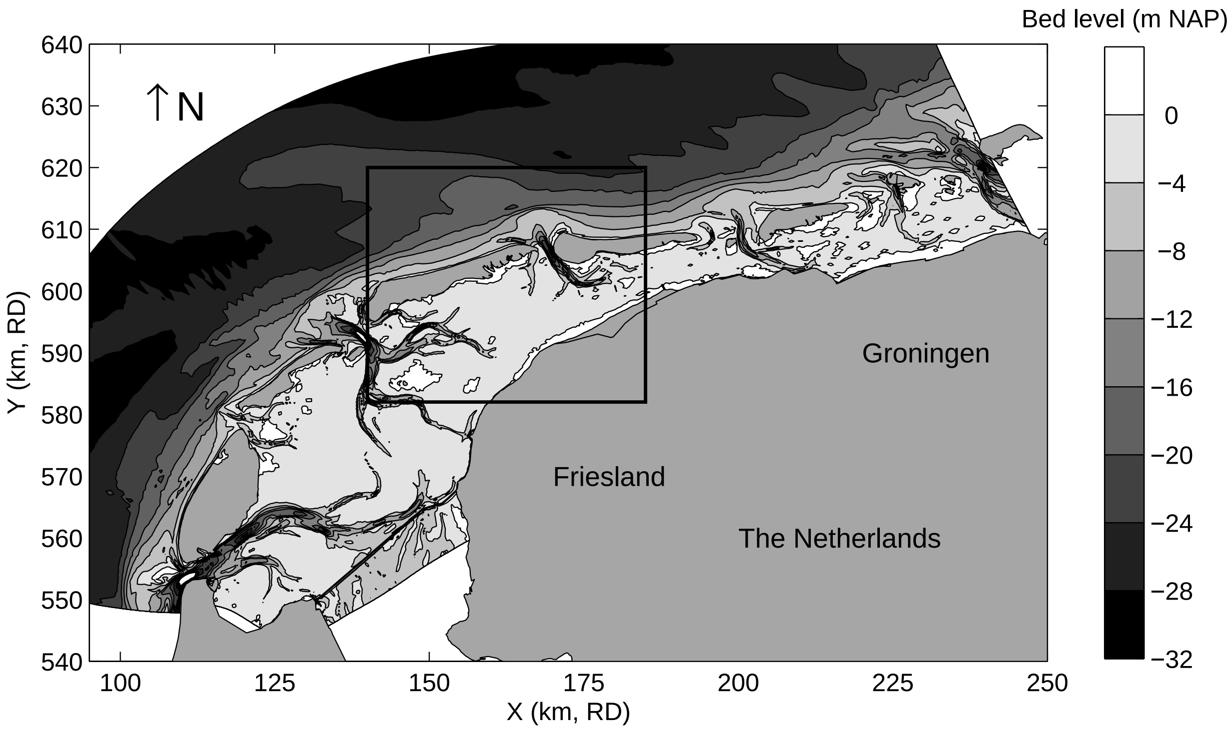
Bed level (m NAP)
0
−4
−8
−12
−16
−20
−24
−28
−32
↑N
Groningen
Friesland
The Netherlands
Y (km, RD)
640
630
620
610
600
590
580
570
560
550
540
X (km, RD)
100
125
150
175
200
225
250

Figure 1.

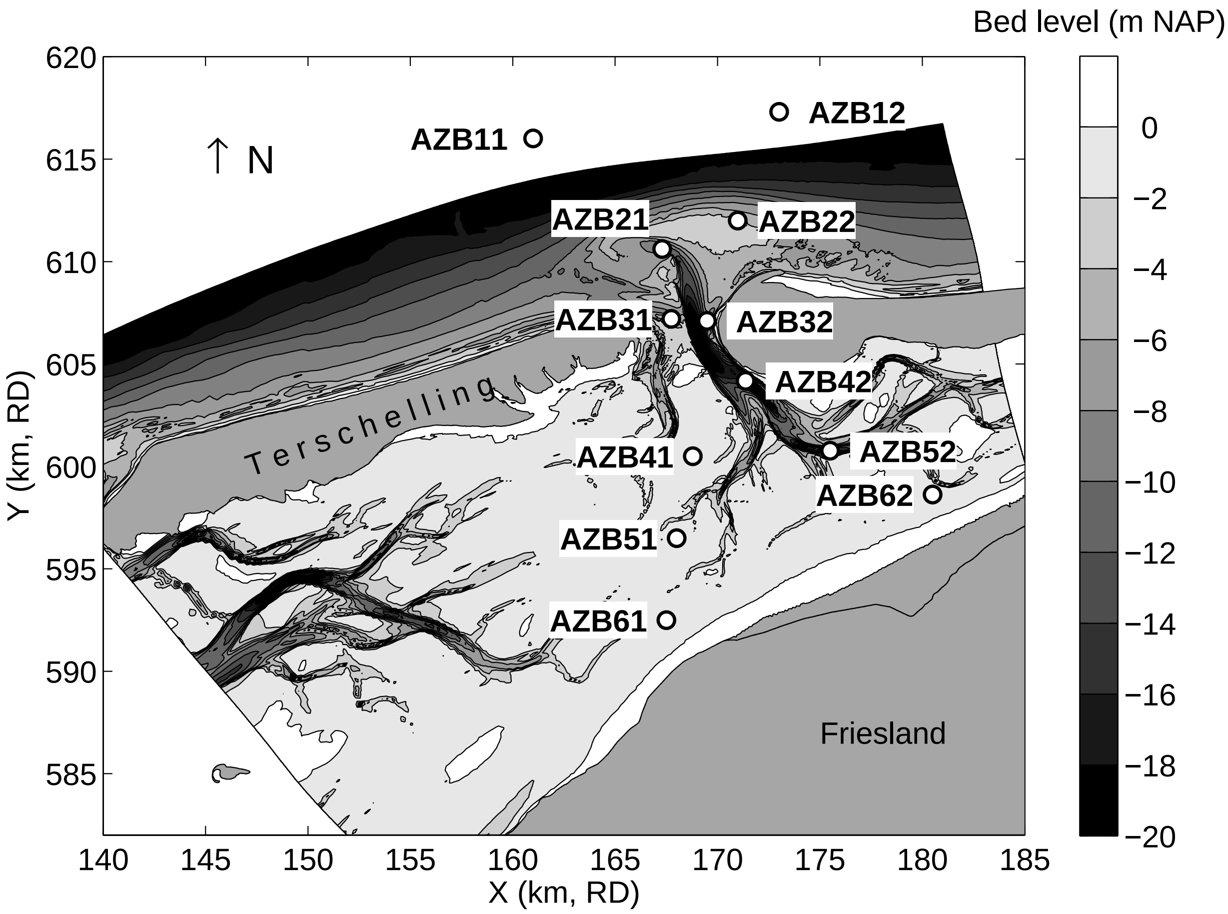
Bed level (m NAP)
0
−2
−4
−6
−8
−10
−12
−14
−16
−18
−20
↑ N
AZB11
AZB12
AZB21
AZB22
AZB31
AZB32
AZB42
AZB41
AZB52
AZB62
AZB51
AZB61
Terschelling
Friesland
620
615
610
605
600
595
590
585
Y (km, RD)
140
145
150
155
160
165
170
175
180
185
X (km, RD)

Figure 2.

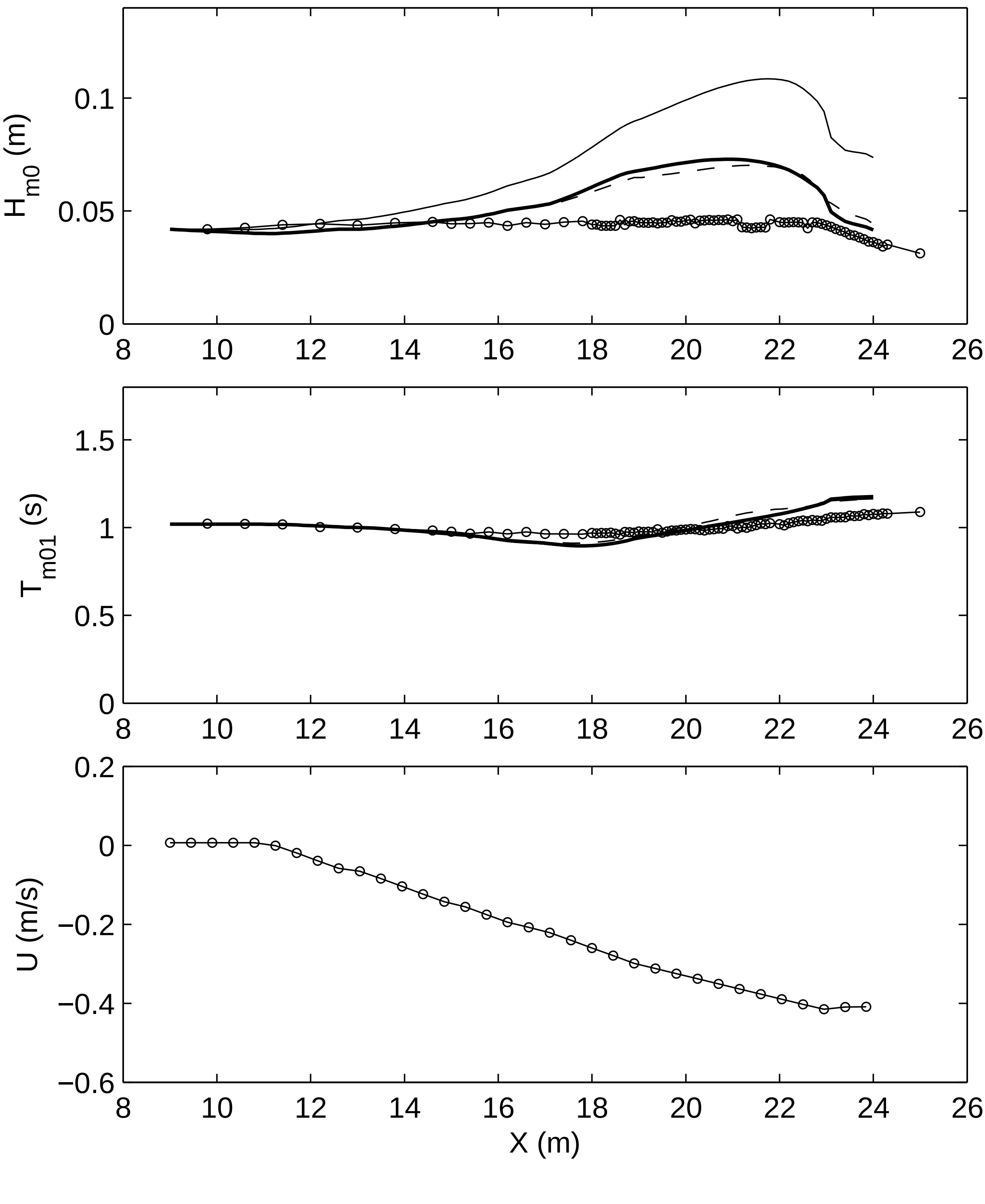
0.1
0.05
0
H_{m0} (m)
8 10 12 14 16 18 20 22 24 26
1.5
1
0.5
0
T_{m01} (s)
8 10 12 14 16 18 20 22 24 26
0.2
0
−0.2
−0.4
−0.6
U (m/s)
8 10 12 14 16 18 20 22 24 26
X (m)

Figure 3.

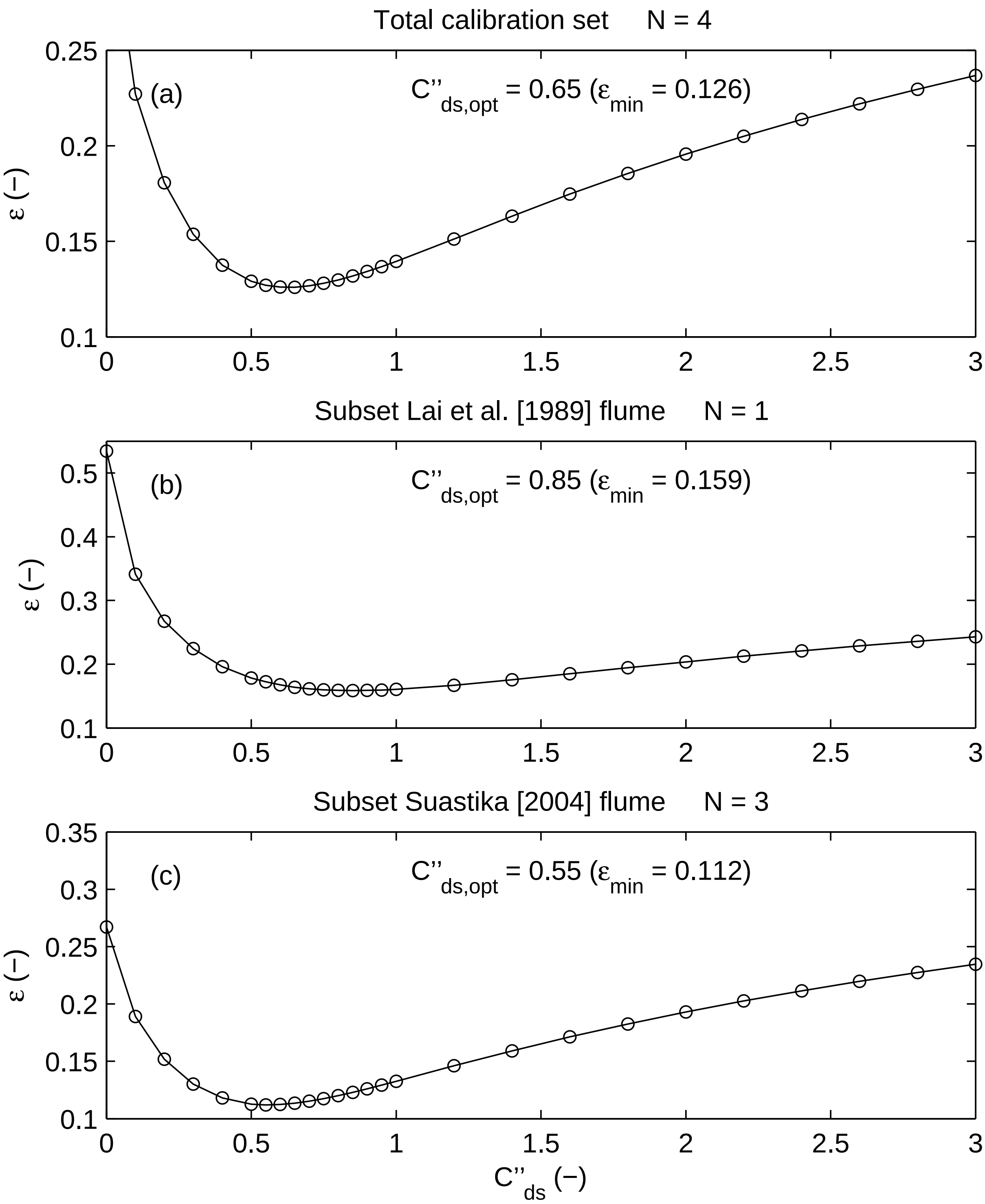
Total calibration set N = 4
(a)
C''ds,opt = 0.65 (εmin = 0.126)
ε (−)
Subset Lai et al. [1989] flume N = 1
(b)
C''ds,opt = 0.85 (εmin = 0.159)
ε (−)
Subset Suastika [2004] flume N = 3
(c)
C''ds,opt = 0.55 (εmin = 0.112)
ε (−)
C''ds (−)

Figure 4.

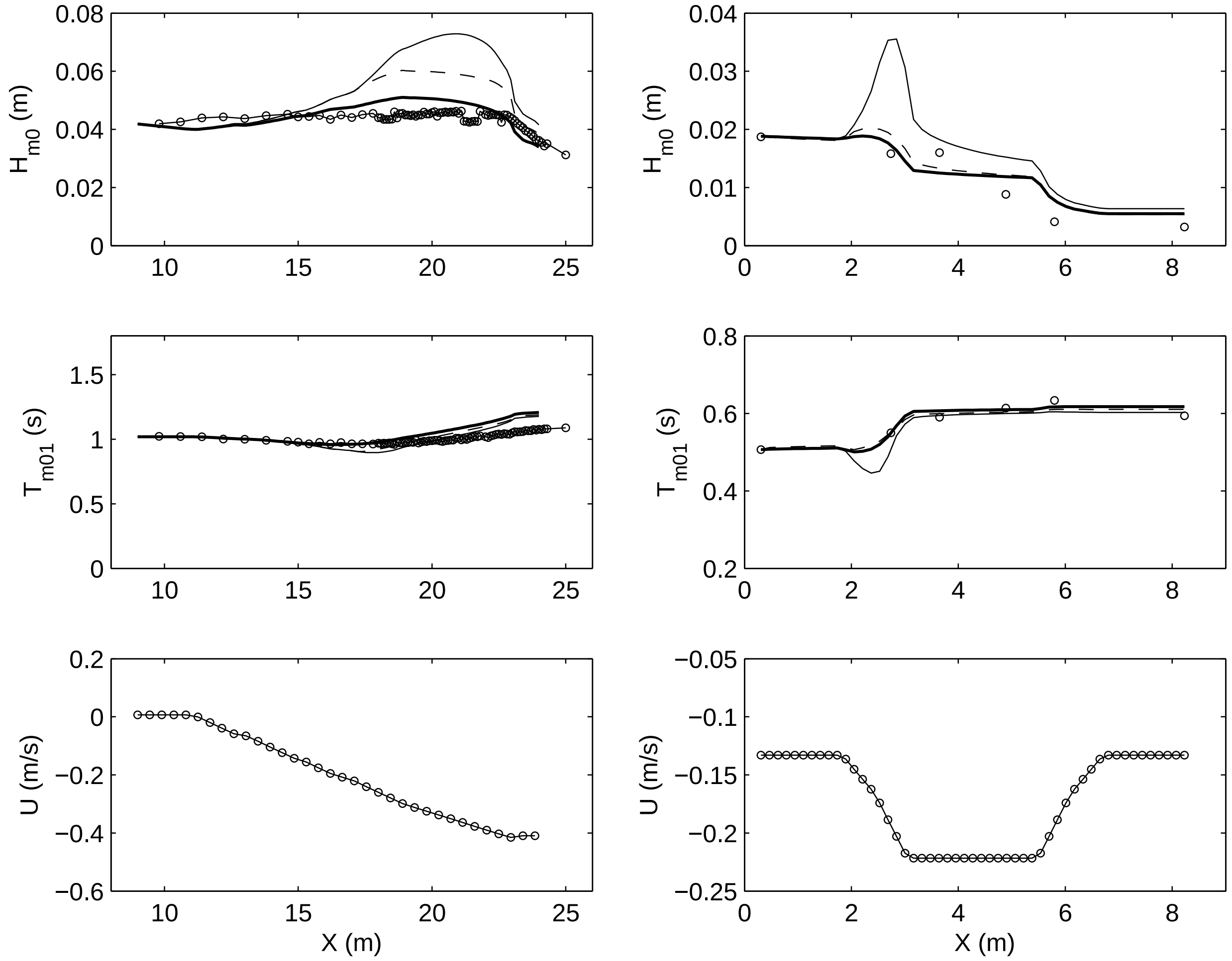
0.08
0.06
0.04
0.02
0
H_{m0} (m)
10
15
20
25
0.04
0.03
0.02
0.01
0
H_{m0} (m)
0
2
4
6
8
1.5
1
0.5
0
T_{m01} (s)
0.8
0.6
0.4
0.2
T_{m01} (s)
0.2
0
−0.2
−0.4
−0.6
U (m/s)
X (m)
−0.05
−0.1
−0.15
−0.2
−0.25
U (m/s)
X (m)

Figure 5.

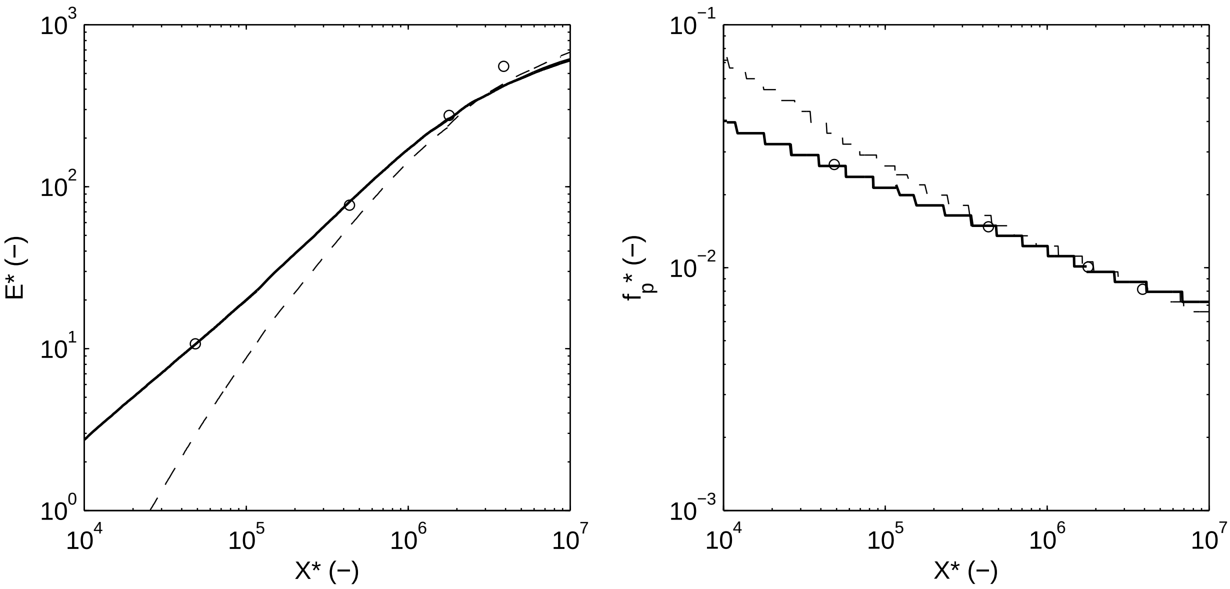
10^3
10^2
10^1
10^0
E* (−)
10^4
10^5
10^6
10^7
X* (−)
10^−1
10^−2
10^−3
f_p* (−)
10^4
10^5
10^6
10^7
X* (−)

Figure 6.

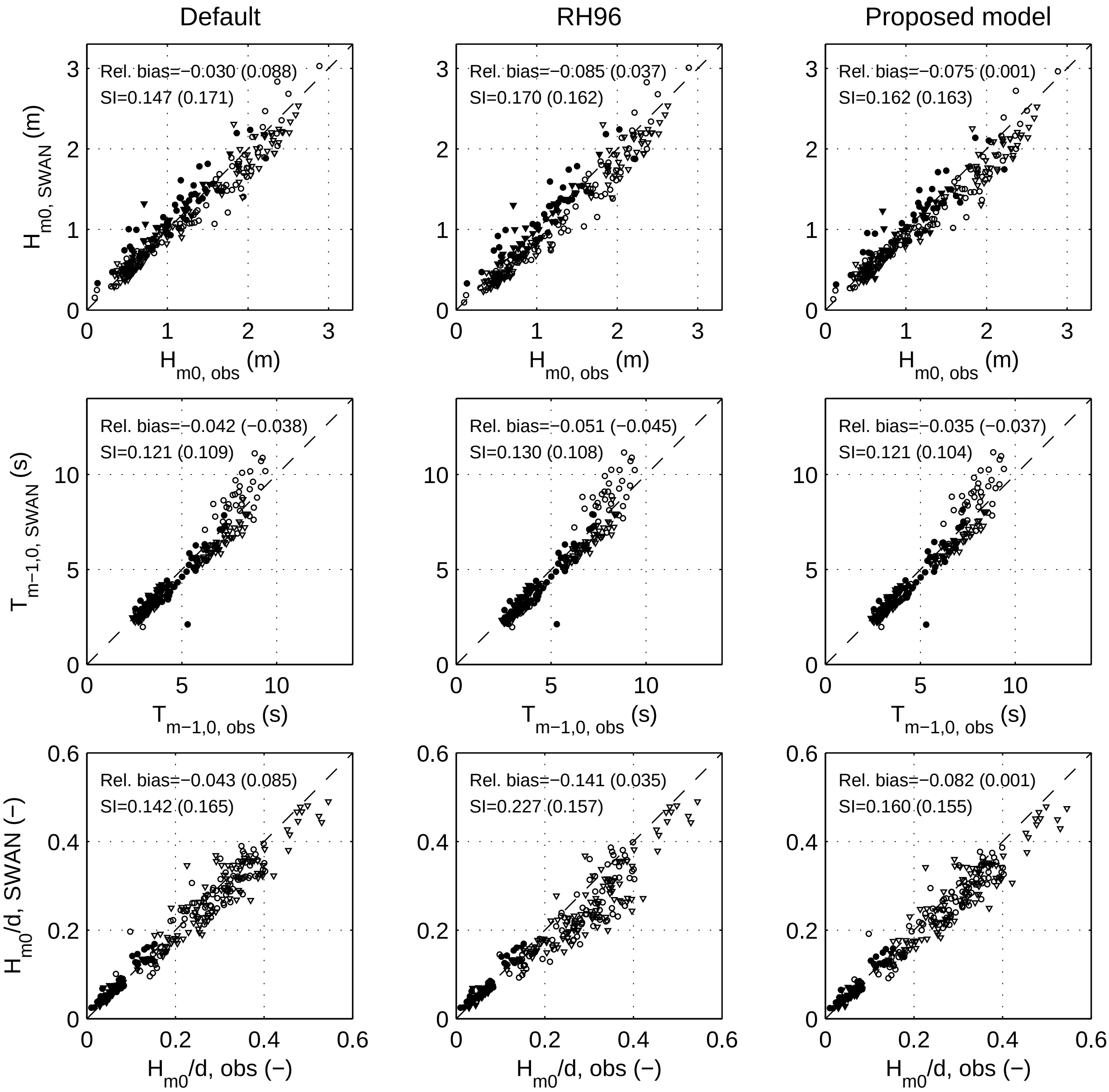
Default
RH96
Proposed model
Rel. bias=−0.030 (0.088)
SI=0.147 (0.171)
Rel. bias=−0.085 (0.037)
SI=0.170 (0.162)
Rel. bias=−0.075 (0.001)
SI=0.162 (0.163)
H m0, SWAN (m)
H m0, obs (m)
Rel. bias=−0.042 (−0.038)
SI=0.121 (0.109)
Rel. bias=−0.051 (−0.045)
SI=0.130 (0.108)
Rel. bias=−0.035 (−0.037)
SI=0.121 (0.104)
T m−1,0, SWAN (s)
T m−1,0, obs (s)
Rel. bias=−0.043 (0.085)
SI=0.142 (0.165)
Rel. bias=−0.141 (0.035)
SI=0.227 (0.157)
Rel. bias=−0.082 (0.001)
SI=0.160 (0.155)
H m0/d, SWAN (−)
H m0/d, obs (−)

Figure 7.

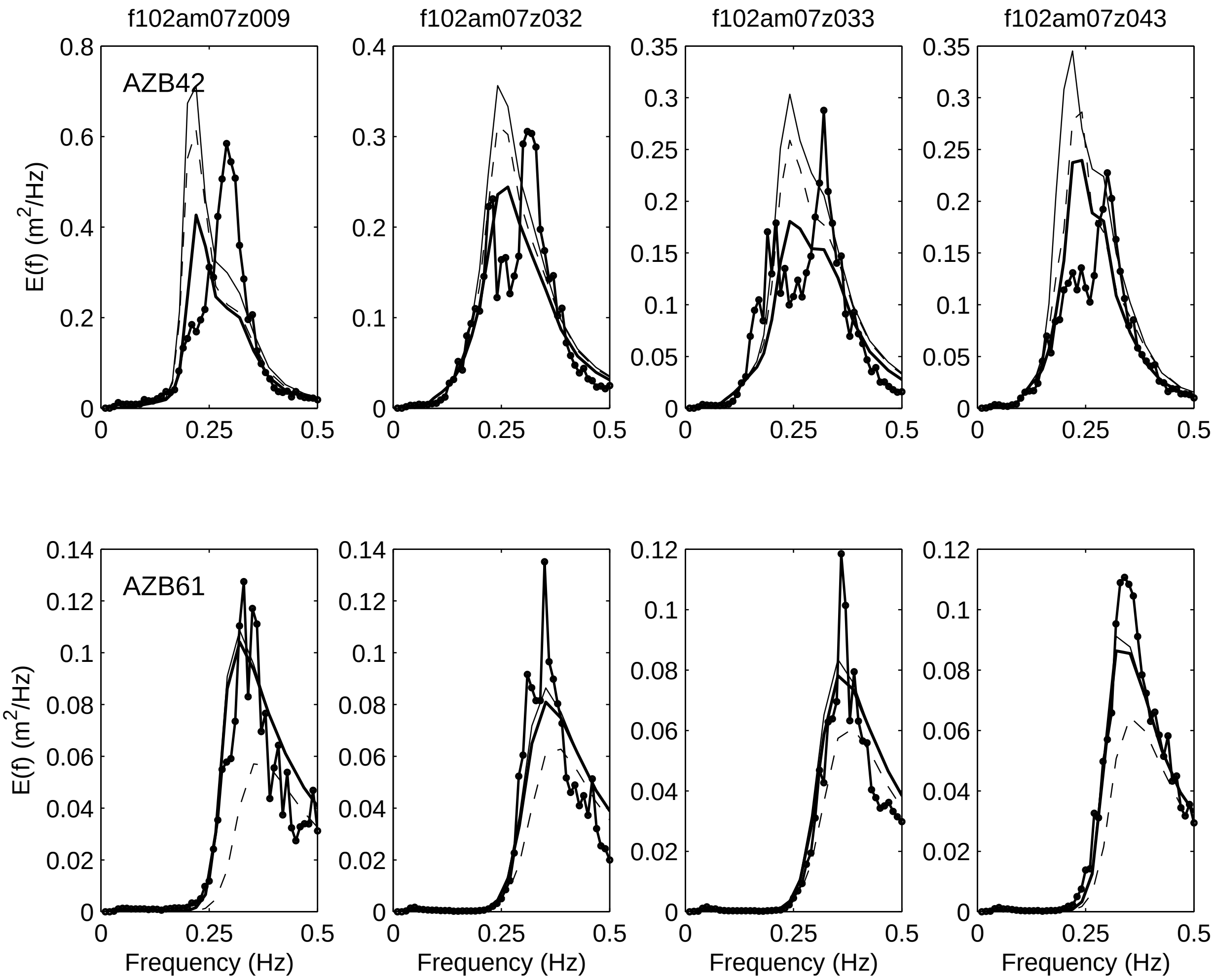
f102am07z009
f102am07z032
f102am07z033
f102am07z043
AZB42
AZB61
E(f) (m^2/Hz)
Frequency (Hz)

Figure 8.

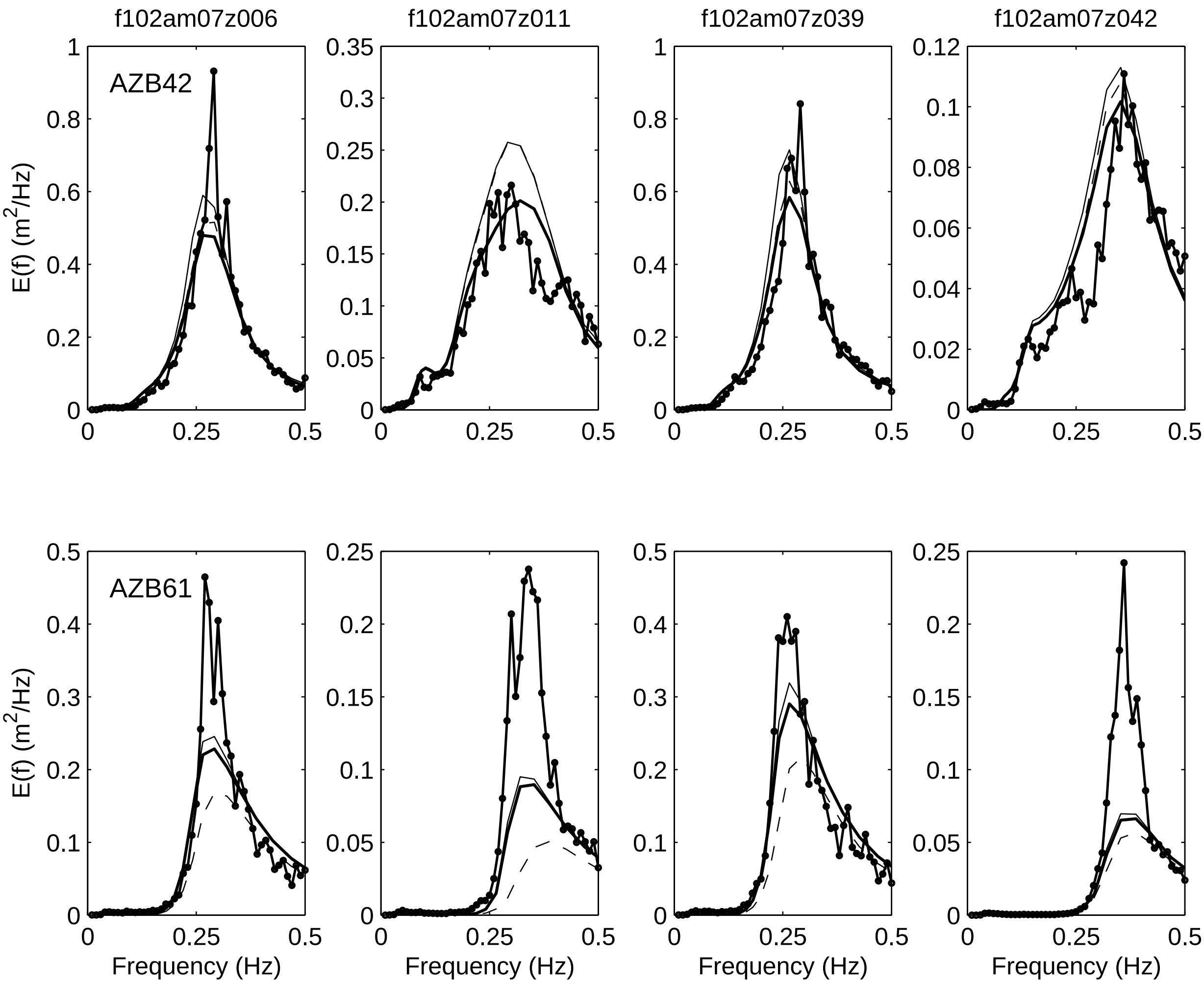
f102am07z006
f102am07z011
f102am07z039
f102am07z042
AZB42
AZB61
E(f) (m2/Hz)
Frequency (Hz)

Figure 9.

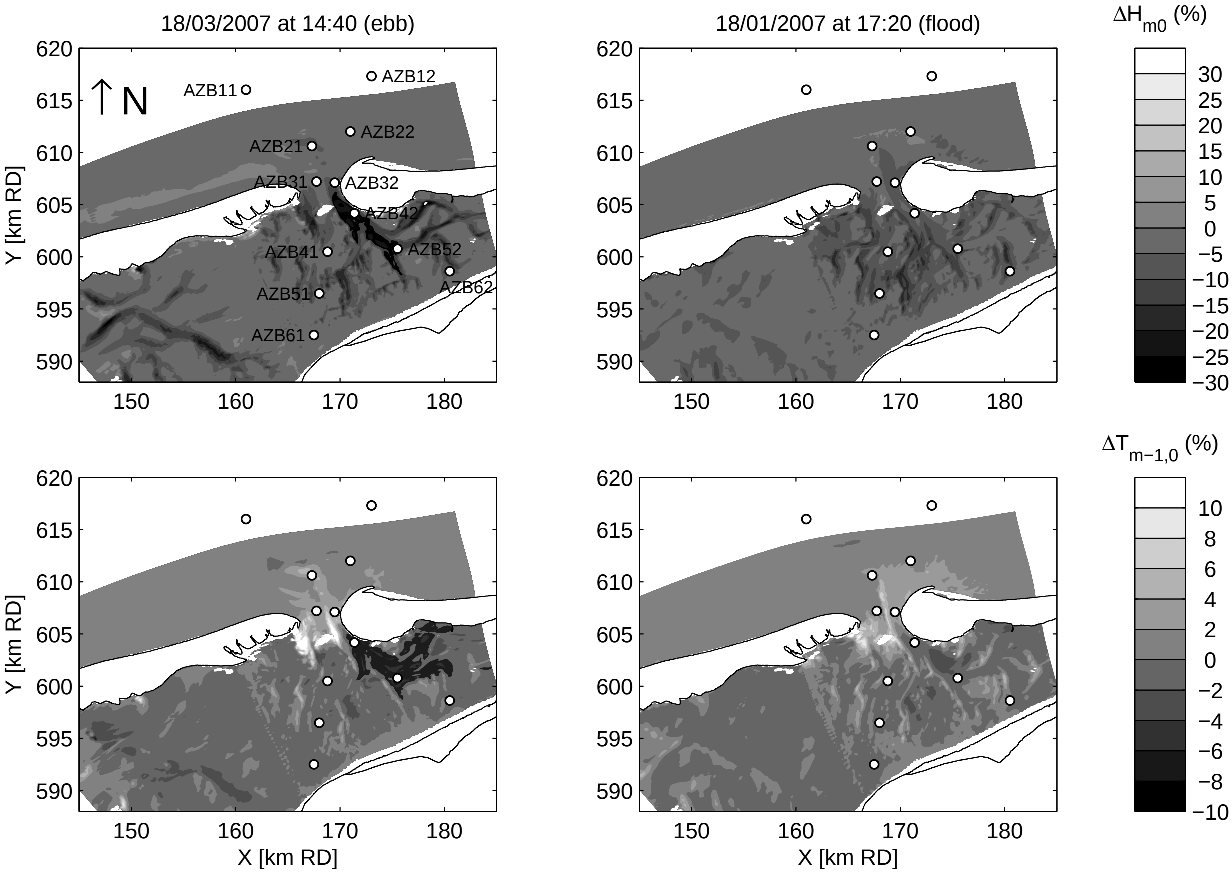

18/03/2007 at 14:40 (ebb)
18/01/2007 at 17:20 (flood)
ΔHm0 (%)
30
25
20
15
10
5
0
−5
−10
−15
−20
−25
−30
↑N
AZB11
AZB12
AZB21
AZB22
AZB31
AZB32
AZB41
AZB42
AZB51
AZB52
AZB61
AZB62
Y [km RD]
X [km RD]
620
615
610
605
600
595
590
150
160
170
180
ΔTm−1,0 (%)
10
8
6
4
2
0
−2
−4
−6
−8
−10

Figure 10.